INTERNATIONAL JOURNAL FOR NUMERICAL METHODS IN ENGINEERING, VOL. 35, 1289–1309 (1992)

COMPUTATIONAL MODEL FOR 3-D CONTACT PROBLEMS WITH FRICTION BASED ON THE PENALTY METHOD

DJORDJE PERIĆ AND D. R. J. OWEN

Department of Civil Engineering, University College of Swansea, Swansea SA2 8PP, Wales, U.K.

SUMMARY

A model based on the penalty method for 3-D contact problems with friction is proposed. The friction forces are assumed to follow the Coulomb law, with a slip criterion treated in the context of a standard return mapping algorithm. Consistent linearization of the field equations is performed which leads to a fully implicit scheme with non-symmetric tangent stiffness which preserves asymptotic quadratic convergence of the Newton–Raphson method. Numerical results are obtained for some representative examples and compared with existing solutions.

1. INTRODUCTION

In the past decade considerable effort has been invested in understanding contact problems with friction, which is evident from the numerous contributions which have appeared (see Reference 34 for an extensive bibliography list), and although a high level of understanding has been achieved, presented, for example, by Kikuchi and Oden,[13] certain problems still await to be solved. This mostly applies to three-dimensional contact problems with friction in the presence of large deformations. Even for non-frictional contact problems, a consistent linearization of the field equations in the Newton–Raphson numerical algorithm leads to intricate expressions (see Reference 32 for two-dimensional and Reference 22 for three-dimensional applications). Recently, non-linear kinematics was included for two-dimensional contact problems with friction by Ju and Taylor[11] and Wriggers *et al.*[33] Problems associated with consistent operators are avoided in explicit algorithms where complicated two- and three-dimensional contact–impact problems have already being solved (see e.g. References 9 and 1).

The aim of this paper is to provide a framework for contact problems with friction, which can be successfully applied for a class of problems where a deformable three-dimensional structure is in frictional contact with rigid bodies of a general three-dimensional shape. By choosing the penalty method we expect successful application for problems not involving high normal forces (e.g. thin sheet metal forming is one possible area of interest). Our main concern is the development of a reliable and efficient numerical algorithm that can deal with a continuous change of the direction and sign of the frictional force. Kinematical non-linearity associated with surface curvatures is avoided through discretization of the rigid body surface by a sufficient number of triangular facet elements.

The layout of the paper is as follows: In Section 3, a framework for the plasticity theory of friction is proposed, based on additive decomposition of the relative tangential velocities into

0029–5981/92/191289–21$15.50

Received 28 March 1991
Revised 17 December 1991

elastic and inelastic parts, i.e. $\dot{\mathbf{g}}_T = \dot{\mathbf{g}}_T^e + \dot{\mathbf{g}}_T^p$. In such a situation, the constitutive equations for contact with friction take the simple format of classical theory of elastoplasticity.

Numerical integration of the constitutive equations relying on operator-split methodology is presented in Section 4. The elastic predictor–plastic corrector procedure is generalized for contact with friction.

Formulation of the complete boundary value problem generalized to large-deformation problems (details may be found in References 23 and 24) and the displacement-based finite element approximation are briefly reviewed in Section 5.

Numerical examples are provided in Section 6. It is shown that the present algorithm can be successfully applied to contact problems in which a continuous change of the direction and sign of the friction forces occurs in large-deformation applications. For the realistic examples of the forming of thin sheet, capabilities are foreseen for the modelling of highly complex processes involving contact with friction.

2. PRELIMINARIES

2.1. Remarks on the computational contact mechanics

We consider the contact problem with friction between two bodies where one is practically non-deformable compared to the other and can be regarded as rigid†, which can be classified as a unilateral contact problem. By disregarding rigid body movements we shall treat the rigid body as fixed in space, which simplifies the notation for interface kinematics.

We define the distance between the bodies as a function

$$g_N = (\boldsymbol{\chi}^s - \boldsymbol{\chi}^m) \cdot \mathbf{N} \quad \text{on} \quad \partial\chi(\Omega_c) = \partial\chi(\Omega^s) \cap \partial\chi(\Omega^m) \tag{1}$$

where g_N is the *gap* between the bodies, $\chi(\Omega^s)$ and $\chi(\Omega^m)$ is the configuration mapping of the slave and master bodies, respectively, and $\mathbf{N}$ is the normal vector on the master surface.

Introducing the notation $p_N = \mathbf{p} \cdot \mathbf{N}$ for the contact force acting on the slave body, the contact condition can be stated in the standard Kuhn–Tucker form

$$g_N \geqslant 0, \quad p_N \leqslant 0, \quad p_N \cdot g_N = 0 \tag{2}$$

which may be viewed as two complementary unilateral constraints: the kinematic condition of no penetration, and the static condition of compressive normal force. Incorporation of form (2) of the contact condition within an appropriate functional, leads to a category of mathematical programming problems of finding the constrained minimum of the appropriate functional, where (1) is the constraint condition and normal forces p_N can be recognized as Lagrange multipliers. A discrete version of the Lagrange multiplier method for three-dimensional contact problems with friction was employed by Chaudhary and Bathe.[3] Apart from an extended number of unknowns, this approach can cause difficulties in the solution phase due to the appearance of zeros on the diagonal of the associated algebraic system. We note that kinematical constraint (1) in this method is exactly satisfied.

By choosing the penalty method the constraint condition (1) is relaxed and the constraint space

$$\mathscr{K} = \{\boldsymbol{\eta} \in \mathscr{V} \mid g_N \geqslant 0 \quad \text{on } \chi(\partial\Omega_c)\} \tag{3}$$

†Following standard terminology (see Reference 9) we shall call the rigid body the *master* body and the deformable body the *slave* body. The same master–slave terminology applies to the surfaces of interest and to the nodes of discretized models.

for which the approximation functions are sometimes difficult to generate, is extended onto the whole space $\mathscr{V}$,

$$\mathscr{V} = \{\boldsymbol{\eta}: \boldsymbol{\chi}(\Omega) \to \mathbb{R}^3 | \boldsymbol{\eta} = \mathbf{0} \quad \text{on } \boldsymbol{\chi}(\partial\Omega_u)\} \tag{4}$$

which allows a classical displacement-based finite element formulation.

Furthermore, the elastoplastic form of the constitutive model for friction described in Section 3, can be viewed as a regularization procedure in which an essentially non-differentiable functional representing the virtual work of the frictional forces is approximated with the regularized one depending upon a real parameter $k_T > 0$ (see Reference 13). This makes numerical techniques, specifically the Newton–Raphson method, effective for this class of problems, as will be shown in Section 6.

The elastoplastic character of the constitutive law for dry friction has a physical justification by relation to the deformation of asperities on contact interfaces, which consists roughly of a reversible part due to elastic deformations of asperities and an irreversible part due to plastic deformation, damage and fracture of asperities. This fact is confirmed by experimental evidence and recognized in recent formulations of frictional laws (see References 6, 8, 12, 13, 18, 26 and 33).

3. PLASTICITY THEORY OF FRICTION

Following standard formalism of the theory of elastoplasticity, additive decomposition of the tangential velocity at the contact interface is adopted, i.e.

$$\dot{\mathbf{g}}_T = \dot{\mathbf{g}}_T^e + \dot{\mathbf{g}}_T^p \tag{5}$$

where $\mathbf{g}_T = (\mathbf{I} - \mathbf{N}\otimes\mathbf{N})\cdot\mathbf{u}$.

Furthermore, a perfect friction law is assumed (in the sense as introduced by Curnier[6]) stating that the friction force is proportional to the normal force and is independent of the other state variables, which leads to the slip criterion

$$\phi = \|\mathbf{p}_T\| + \nu_F\|\mathbf{p}_N\| - r \tag{6}$$

where r characterizes the adhesion.

With these assumptions introduced, the constitutive equations for frictional contact take the simple format of classical elastoplasticity

$$\dot{\mathbf{g}}_T = \dot{\mathbf{g}}_T^e + \dot{\mathbf{g}}_T^p \tag{7a}$$

$$\mathbf{p}_N = \mathbf{D}_N\mathbf{u}^e \tag{7b}$$

$$\mathbf{p}_T = \mathbf{D}_T\mathbf{u}^e, \tag{7c}$$

$$\dot{\mathbf{g}}_T^p = \dot{\gamma}\frac{\partial\psi(\mathbf{p}, r)}{\partial\mathbf{p}_T} \tag{7d}$$

$$\dot{r} = \dot{\gamma}h(\mathbf{g}_T^p, r) \tag{7e}$$

Here, $\mathbf{D}_T = -k_T(\mathbf{I} - \mathbf{N}\otimes\mathbf{N})$ and $\mathbf{D}_N = -k_N\mathbf{N}\otimes\mathbf{N}$ are the tangential and normal parts of the elastic modulus tensor, $\psi(\mathbf{p}, r)$ is the slip potential and the function $h(\mathbf{g}_T^p, r)$ defines the hardening (softening) law. Finally, loading/unloading conditions may be formulated in the standard Kuhn–Tucker form

$$\phi \leqslant 0, \quad \dot{\gamma} \geqslant 0, \quad \dot{\gamma}\phi = 0 \tag{8}$$

For convenience, the basic equations governing the constitutive model for the plasticity theory of friction have been summarized in Table I.

Table I. Constitutive model for the plasticity theory of friction

(i) Additive decomposition of the displacement rate

$$\dot{\mathbf{g}}_T = \dot{\mathbf{g}}_T^e + \dot{\mathbf{g}}_T^p$$

(ii) Linear constitutive equation

$$\dot{\mathbf{p}}_N = \mathbf{D}_N \dot{\mathbf{u}}_N^e, \quad \mathbf{D}_N = -k_N \mathbf{N}\otimes\mathbf{N}$$

$$\dot{\mathbf{p}}_T = \mathbf{D}_T \dot{\mathbf{u}}_T^e, \quad \mathbf{D}_T = -k_T(\mathbf{I} - \mathbf{N}\otimes\mathbf{N})$$

(iii) Slip criterion and hardening law

$$\phi(\mathbf{p}, r) = \|\mathbf{p}_T\| + v_F\|\mathbf{p}_N\| - r$$

$$\dot{r} = \dot{\gamma} h(\mathbf{g}_T^p, r)$$

(iv) Flow surface and flow rule

$$\psi(\mathbf{p}, r) = \|\mathbf{p}_T\| - r$$

$$\dot{\mathbf{g}}_T^p = \dot{\gamma}\mathbf{T}, \quad \mathbf{T} = \frac{\mathbf{p}_T}{\|\mathbf{p}_T\|}$$

(v) Kuhn–Tucker loading/unloading conditions

$$\phi \leqslant 0, \quad \dot{\gamma} \geqslant 0, \quad \dot{\gamma}\phi = 0$$

Following standard arguments of rate-independent plasticity and under conditions of frictional slip without hardening, the following rate form is obtained

$$\dot{\mathbf{p}} = \mathbf{D}^{ep} \cdot \dot{\mathbf{u}} \tag{9}$$

where

$$\mathbf{D}^{ep} = -k_T(\mathbf{I} - \mathbf{T}\otimes\mathbf{T} - \mathbf{N}\otimes\mathbf{N}) - v_F k_N \mathbf{T}\otimes\mathbf{N} - k_N \mathbf{N}\otimes\mathbf{N} \tag{10}$$

Evidently, the non-associative slip rule (7d) results in *non-symmetry* of the slip modulus tensor which is defined by (10) under the conditions of frictional slip.

4. NUMERICAL INTEGRATION ALGORITHM

By making the contact problem with friction equivalent to the classical theory of elastoplasticity in Section 3, numerical integration of the constitutive equations for frictional contact problems may follow the standard techniques employed in elastoplasticity. We refer to References 28, 30 and 19, for a discussion on the recent advances and details of implementation. For completeness, the equations governing a one-step Euler backward scheme are summarized:

$$\left.\begin{aligned} \Delta\mathbf{g}_T &= \Delta\mathbf{g}_T^e + \Delta\mathbf{g}_T^p \\ \mathbf{p}_{n+1} &= \mathbf{D}\mathbf{u}_{n+1}^e \\ \mathbf{g}_{T_{n+1}}^p &= \mathbf{g}_{T_n}^p + \Delta\gamma \frac{\partial\psi(\mathbf{p}_{n+1}, r_{n+1})}{\partial\mathbf{p}_{T_{n+1}}} \\ r_{n+1} &= r_n + \Delta\gamma h(\mathbf{g}_{T_{n+1}}^p, r_{n+1}) \end{aligned}\right\} \tag{11}$$

In addition, the constraint condition

$$\phi(\mathbf{p}_{n+1}, r_{n+1}) = 0$$

must be satisfied.

4.1. Stress update algorithm

Particularly suitable for implementation are procedures connected with general operator-split methodology, where the original problem of evolution is solved through composition, applying first the elastic and then the plastic algorithm. We summarize the basic equations for the radial return method proposed by Wilkins,[31] restricting attention to non-hardening frictional slip which is particularly interesting as it defines the generalized Coulomb law of friction.

- *Elastic predictor*
  Calculating increments of displacement in the contact region $\chi(\Omega_c)$, we obtain trial elastic forces

$$\mathbf{p}_{n+1}^{\text{trial}} = \mathbf{p}_n + \mathbf{D}\cdot\mathbf{u}_{n+1} \tag{12}$$

- *Plastic corrector*
  In the plastic corrector phase, a trial elastic stress $\mathbf{p}_{n+1}^{\text{trial}}$ is radially projected onto the slip surface

$$\mathbf{p}_{\mathbf{T}_{n+1}} = \nu_F \| \mathbf{p}_{\mathbf{N}_{n+1}}^{\text{trial}} \| \mathbf{T}_{n+1} \tag{13}$$

  where the normal

$$\mathbf{T}_{n+1} = \frac{\mathbf{p}_{\mathbf{T}_{n+1}}^{\text{trial}}}{\| \mathbf{p}_{\mathbf{T}_{n+1}}^{\text{trial}} \|} \tag{14}$$

  defines the slip direction.

4.2. Consistent tangent operator

The numerical updating procedure described in Section 2.1 leads to the incremental response function

$$\tilde{\mathbf{p}}(\mathbf{p}_n, \mathbf{u}_n, \mathbf{u} - \mathbf{u}_n) = \| \mathbf{p}_{\mathbf{T}_{n+1}} \| \mathbf{T}_{n+1} + \| \mathbf{p}_{\mathbf{N}_{n+1}} \| \mathbf{N}_{n+1} \tag{15}$$

Making use of the relationship

$$\frac{\partial \mathbf{T}_{n+1}}{\partial \mathbf{p}_{\mathbf{T}_{n+1}}^{\text{trial}}} = \frac{1}{\| \mathbf{p}_{\mathbf{T}_{n+1}}^{\text{trial}} \|} (\mathbf{I} - \mathbf{T}_{n+1} \otimes \mathbf{T}_{n+1}) \tag{16}$$

and applying the chain rule of differentiation in

$$\mathbf{D}^{*\,\text{ep}} = \left. \frac{\partial \tilde{\mathbf{p}}(\mathbf{p}_n, \mathbf{u}_n, \mathbf{u} - \mathbf{u}_n)}{\partial \mathbf{u}} \right|_{\mathbf{u} = \mathbf{u}_{n+1}} \tag{17}$$

we obtain the *consistent tangent modulus* for frictional slip

$$\mathbf{D}^{*\,\text{ep}} = -k_T^*(\mathbf{I} - \mathbf{T}_{n+1} \otimes \mathbf{T}_{n+1} - \mathbf{N}_{n+1} \otimes \mathbf{N}_{n+1}) - \nu_F k_N \mathbf{T}_{n+1} \otimes \mathbf{N}_{n+1} - k_N \mathbf{N}_{n+1} \otimes \mathbf{N}_{n+1} \tag{18}$$

where

$$k_T^* = k_T \frac{\| \mathbf{p}_{\mathbf{T}_{n+1}} \|}{\| \mathbf{p}_{\mathbf{T}_{n+1}}^{\text{trial}} \|} \tag{19}$$

Observe that the consistent modulus (18) differs from the continuum tangent modulus (10) by the factor k_T^* which reduces the stiffness in the tangential plane perpendicular to the slip direction. For large displacement increments k_T^* can become considerably less than k_T, i.e. $k_T^* \ll k_T$, so that

use of k_T instead of k_T^* may cause loss of the quadratic rate of convergence typical for the Newton–Raphson method.

The algorithm is summarized in Box 1.

Box 1. Numerical integration procedure for the plasticity theory of friction

- Update configuration

$$\chi_{n+1} = \chi_{n+1}^{(i)} + \mathbf{u}_{n+1}^{(i)}$$

- Elastic stress

$$\mathbf{p}_{n+1}^{\text{trial}} = \mathbf{p}_n + \mathbf{D} \cdot \mathbf{u}_{n+1}$$

- Check for slipping

$$\text{IF } \phi_{n+1}^{\text{trial}} = \| \mathbf{p}_{T_{n+1}}^{\text{trial}} \| + v_F \| \mathbf{p}_{N_{n+1}}^{\text{trial}} \| \leqslant 0$$

Set $(\bullet)_{n+1} = (\bullet)_{n+1}^{\text{trial}}$ then EXIT

ELSE

- Plastic corrector phase

$$\mathbf{T}_{n+1} = \frac{\mathbf{p}_{T_{n+1}}^{\text{trial}}}{\| \mathbf{p}_{T_{n+1}}^{\text{trial}} \|}$$

$$\mathbf{p}_{T_{n+1}} = v_F \| \mathbf{p}_{N_{n+1}}^{\text{trial}} \| \mathbf{T}_{n+1}$$

- Compute *consistent* frictional slip tangent moduli

$$\mathbf{D}^{*ep} = -k_T^* (\mathbf{I} - \mathbf{T}_{n+1} \otimes \mathbf{T}_{n+1} - \mathbf{N}_{n+1} \otimes \mathbf{N}_{n+1}) - v_F k_N \mathbf{T}_{n+1} \otimes \mathbf{N}_{n+1} - k_N \mathbf{N}_{n+1} \otimes \mathbf{N}_{n+1}$$

$$k_T^* = k_T \frac{\| \mathbf{p}_{T_{n+1}} \|}{\| \mathbf{p}_{T_{n+1}}^{\text{trial}} \|}$$

Remark 1. The consistent tangent modulus (18) is equivalent to the consistent modulus obtained by Curnier and Alart[7] through kinematic considerations.

5. FORMULATION OF THE BOUNDARY VALUE PROBLEM AND FINITE ELEMENT DISCRETIZATION

In this section we present a variational formulation for large-deformation problems in the presence of large strains and unilateral contact with friction, as a basis for finite element discretization. As has been usually done in metal plasticity, we chose a logarithmic strain as the strain measure (see Reference 24 for details concerning the utilization of the logarithmic strain in finite strain elastoplasticity). Restriction to unilateral contact allows use of linear contact kinematics, which greatly simplifies the treatment of three-dimensional problems and leads to rank-one updates of the tangent stiffness according to equations (9) and (10).

5.1. Weak form of the boundary value problem

The *strong form* of the boundary value problem, written in *spatial description*

$$\operatorname{div}\boldsymbol{\sigma} + \rho\bar{\mathbf{b}} = 0 \quad \text{in } \boldsymbol{\chi}(\Omega) \tag{20}$$

with boundary conditions

$$\left.\begin{aligned} \boldsymbol{\sigma}\cdot\mathbf{n} &= \bar{\mathbf{t}} \quad \text{on } \partial\boldsymbol{\chi}(\Omega_\sigma) \\ \boldsymbol{\chi} &= \bar{\boldsymbol{\chi}} \quad \text{on } \partial\boldsymbol{\chi}(\Omega_u) \\ \boldsymbol{\sigma}\cdot\mathbf{n} &= \mathbf{0} \quad \text{if } g_N > 0, \quad \text{on } \partial\boldsymbol{\chi}(\Omega_c) \end{aligned}\right\} \tag{21}$$

and

$$\boldsymbol{\sigma}\cdot\mathbf{n} = \mathbf{p} \quad \text{if } g_N \leqslant 0, \quad \text{on } \partial\boldsymbol{\chi}(\Omega_c)$$

takes the classical *weak form* (see Reference 16)

$$G(\chi, \boldsymbol{\eta}) = \int_{\chi(\Omega)} (\boldsymbol{\sigma}:\nabla\boldsymbol{\eta} - \rho\bar{\mathbf{b}}\cdot\boldsymbol{\eta})\,dv - \int_{\chi(\partial\Omega_\sigma)} \bar{\mathbf{t}}\cdot\boldsymbol{\eta}\,da - \int_{\chi(\partial\Omega_c)} \mathbf{p}\cdot\boldsymbol{\eta}\,da \tag{22}$$

where $\boldsymbol{\eta}\in\mathscr{V}$ and $\mathscr{V}$ is the space of all *admissible variations.*

The linearized form of the functional $G(\boldsymbol{\chi}, \boldsymbol{\eta})$ at the known configuration $\boldsymbol{\chi} = \hat{\boldsymbol{\chi}}$ in the spatial description may be written (see Reference 24 for details) as

$$\int_{\chi(\Omega)} \nabla\mathbf{u}:\mathbf{a}^{(0)}:\nabla\boldsymbol{\eta}\,dv + \int_{\chi(\partial\Omega_c)} \mathbf{u}:\mathbf{D}:\boldsymbol{\eta}\,da = -G(\hat{\boldsymbol{\chi}}, \boldsymbol{\eta}) \tag{23}$$

where $\mathbf{a}^{(0)}$ is the fourth-order tensor given by

$$\mathsf{a}^{(0)}_{ijkl} = \mathsf{h}^{(0)\,ep}_{ijkl} - \mathsf{m}_{ijkl} + \delta_{ik}\sigma_{jl} \tag{24}$$

with $\mathbf{h}^{(0)\,ep}$ as the standard elastoplastic constitutive moduli and

$$\mathsf{m}_{ijkl} = \tfrac{1}{2}(\sigma_{ik}\delta_{jl} + \sigma_{il}\delta_{jk} + \sigma_{jk}\delta_{il} + \sigma_{jl}\delta_{ik}) \tag{25}$$

The term $G(\hat{\boldsymbol{\chi}}, \boldsymbol{\eta})$ has a standard interpretation as an *unbalanced force* at the configuration $\hat{\boldsymbol{\chi}}$, while the terms on the left-hand side of the equation (23), linear in $\mathbf{u}$, provide the *tangent stiffness.*

From $\int_{\chi(\Omega)} \nabla\mathbf{u}:\mathbf{a}^{(0)}:\nabla\boldsymbol{\eta}\,dv$ we recover the *material* and *geometrical* parts of the tangent stiffness, respectively:

$${}^{M}K = \int_{\chi(\Omega)} \nabla^s\mathbf{u}:(\mathbf{h}^{(0)\,ep} - \mathbf{m}):\nabla^s\boldsymbol{\eta}\,dv \tag{26}$$

$${}^{G}K = \int_{\chi(\Omega)} \nabla\mathbf{u}:(\boldsymbol{\sigma}\otimes\mathbf{1}):\nabla\boldsymbol{\eta}\,dv \tag{27}$$

where ∇^s denotes the symmetric part of ∇. The term

$${}^{C}K = \int_{\chi(\partial\Omega_c)} \mathbf{u}\cdot\mathbf{D}^{ep}\cdot\boldsymbol{\eta}\,da \tag{28}$$

provides the tangent stiffness due to *frictional contact.*

Analogously, we obtain the *residual forces* as

$$\hat{G} = \int_{\chi(\Omega)} \hat{\boldsymbol{\sigma}}:\nabla^s\boldsymbol{\eta}\,dv - {}^{EXT}\hat{G} \tag{29}$$

where ${}^{\mathrm{EXT}}\hat{G}$ is the virtual work of the external loading and contact forces

$$ {}^{\mathrm{EXT}}\hat{G} = \int_{\chi(\Omega)} \rho\bar{\mathbf{b}}\cdot\boldsymbol{\eta}\,\mathrm{d}v + \int_{\chi(\partial\Omega_\sigma)} \bar{\mathbf{t}}\cdot\boldsymbol{\eta}\,\mathrm{d}a + \int_{\chi(\partial\Omega_c)} \mathbf{p}\cdot\boldsymbol{\eta}\,\mathrm{d}a \tag{30} $$

5.2. *Finite element discretization*

Following a standard methodology (see References 2, 10 or 35), we introduce the space $\mathscr{V}^h \subset \mathscr{V}$ as a finite-dimensional approximation to $\mathscr{V}$ described in equation (4). Furthermore, let subspace $\mathscr{V}^h$ be generated through spatial finite element discretization in the current configuration $\chi(\Omega) = \cup_{e=1}^{\mathrm{NEL}} \chi(\Omega_e)$, with $\chi(\Omega_a) \cap \chi(\Omega_b) = \emptyset$ if $a \neq b$, so that over a typical element $\chi(\Omega_e)$ we have the interpolation

$$ \mathbf{u}^h|_{\chi(\Omega_e)} = \sum_{a=1}^{\mathrm{NEN}} \mathbf{N}_a(\mathbf{x})\,\mathbf{u}_a \tag{31} $$

where $\mathbf{N}_a$ are the standard shape functions.

Contact conditions are discretized by controlling the penetration of the slave nodes into the master surface. Further simplification is introduced by monitoring only the nodal forces developed due to frictional contact, which are assumed to follow the constitutive model described in Sections 3 and 4.

Tangent stiffness matrix. Representing the discrete gradient operators $\nabla^s\mathbf{u}^h$ and $\nabla\mathbf{u}^h$ in the form

$$ \nabla^s\mathbf{u}^h|_{\chi(\Omega_e)} = \sum_{a=1}^{\mathrm{NEN}} \mathbf{B}_a\mathbf{u}_a, \quad \nabla\mathbf{u}^h|_{\chi(\Omega_e)} = \sum_{a=1}^{\mathrm{NEN}} \mathbf{G}_a\mathbf{u}_a \tag{32} $$

we may write the tangent operator of equations (26) and (27) in the *matrix format*

$$ \mathbf{k}^e = {}^{\mathrm{M}}\mathbf{k}^e + {}^{\mathrm{G}}\mathbf{k}^e \tag{33} $$

where

$$ {}^{\mathrm{M}}\mathbf{k}^e = [{}^{\mathrm{M}}\mathbf{k}^e_{ab}] = \int_{\chi(\Omega_e)} \mathbf{B}_a^{\mathrm{T}}[\mathbf{h}^{(0)\mathrm{ep}} - \mathbf{m}]\,\mathbf{B}_b\,\mathrm{d}v \tag{34} $$

$$ {}^{\mathrm{G}}\mathbf{k}^e = [{}^{\mathrm{G}}\mathbf{k}^e_{ab}] = \int_{\chi(\Omega_e)} \mathbf{G}_a^{\mathrm{T}}[\hat{\boldsymbol{\sigma}}]\,\mathbf{G}_b\,\mathrm{d}v \tag{35} $$

are the standard *material* and *geometrical* element stiffness matrices, respectively. A discrete version of equation (28) follows directly from equation (18):

$$ {}^{\mathrm{C}}\mathbf{K}^s = \mathbf{D}^{*\mathrm{ep}} \tag{36} $$

The global stiffness matrix is obtained by applying the finite element assembly operator[10]

$$ \mathbf{K} = \mathop{\mathbf{A}}_{e=1}^{\mathrm{NEL}} (\mathbf{k}^e) + \mathop{\mathbf{A}}_{s=1}^{\mathrm{SNOD}} ({}^{\mathrm{C}}\mathbf{K}^s) \tag{37} $$

Residual vector. The discrete version of equations (29) and (30) supplies the element residual force vector

$$ \mathbf{f}^e = {}^{\mathrm{INT}}\mathbf{f}^e - {}^{\mathrm{EXT}}\mathbf{f}^e \tag{38} $$

where

$$^{\mathrm{INT}}\mathbf{f}^e = \{^{\mathrm{INT}}\mathbf{f}_a^e\} = \int_{\chi(\Omega_e)} \mathbf{B}_a^{\mathrm{T}} \{\hat{\boldsymbol{\sigma}}\}\, \mathrm{d}v, \tag{39}$$

$$^{\mathrm{EXT}}\mathbf{f}^e = \{^{\mathrm{EXT}}\mathbf{f}_a^e\} = \int_{\chi(\Omega_e)} \mathbf{N}_a\{\rho\bar{\mathbf{b}}\}\, \mathrm{d}v + \int_{\chi(\partial\Omega_e)} \mathbf{N}_a\{\bar{\mathbf{t}}\}\, \mathrm{d}a \tag{40}$$

are the element *internal* and *external* force vectors, respectively. The global *residual vector* is obtained by adding the contribution of the contact forces at the slave nodes

$$\mathbf{F} = \mathbf{F}_{\mathrm{nodal}} + \overset{\mathrm{NEL}}{\underset{e=1}{\mathbf{A}}} (\mathbf{f}^e) + \overset{\mathrm{SNOD}}{\underset{s=1}{\mathbf{A}}} (^{\mathrm{C}}\mathbf{F}^s) \tag{41}$$

6. NUMERICAL EXAMPLES

In this section several numerical examples are presented to assess the accuracy and robustness of the constitutive model and the numerical scheme adopted. All problems presented include large deformations and offer a severe test for any computational model dealing with frictional contact.

In all examples a full Newton–Raphson method is employed, with unsymmetric tangent stiffness arising from the non-associated frictional contact law described in Section 3. Convergence of the finite element solution is established on the basis of the standard Euclidean norm of the out-of-balance forces. The use of consistent tangent moduli [equations (18) and (19)] is shown to be of utmost importance for preserving the quadratic rate of convergence typical for the Newton–Raphson method.

Example 1. Lateral compression of a cantilever beam subject to end moment

A straight beam clamped at one end and subject to an end moment at the other is laterally compressed by frictional flat rigid punches which are moved in the first loading increment by $|U_2| = 0{\cdot}004$ on both lateral sides of the beam and then kept fixed. The geometry, material characterization and finite element model are given in Figure 1. The beam is modelled with 20

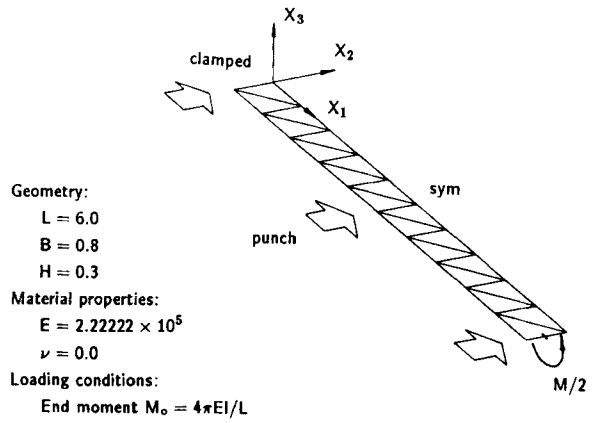

Figure 1. Lateral compression of a cantilever beam subject to end moment: geometry, material characteristics and finite element discretization

triangular constant membrane strain–constant curvature shell elements with symmetry employed along the central axis. The coefficient of friction ν_F at the interface between the beam and punches is varied between 0·0 and 0·3. An applied moment $M_0 = 4\pi EI/L$ will force the beam to deform into a full closed circle for $\nu_F = 0{\cdot}0$. The final deformed configurations for various coefficients of

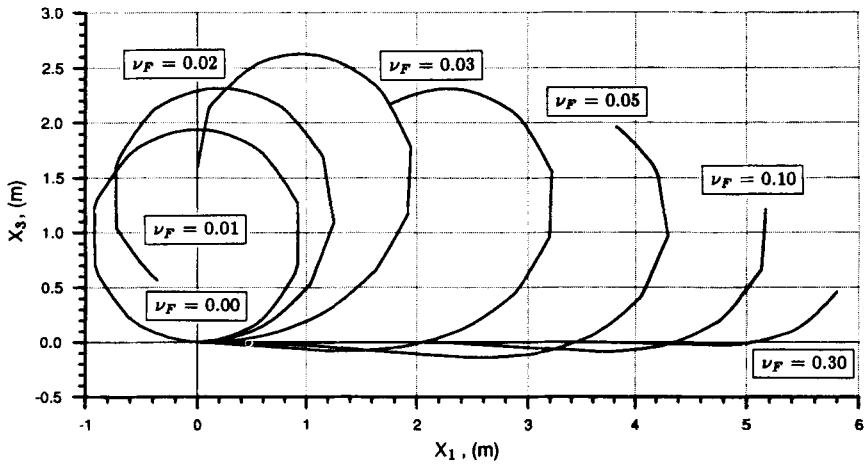

Figure 2. Lateral compression of a cantilever beam subject to end moment: Deformed configurations for $M/M_0 = 1{\cdot}00$

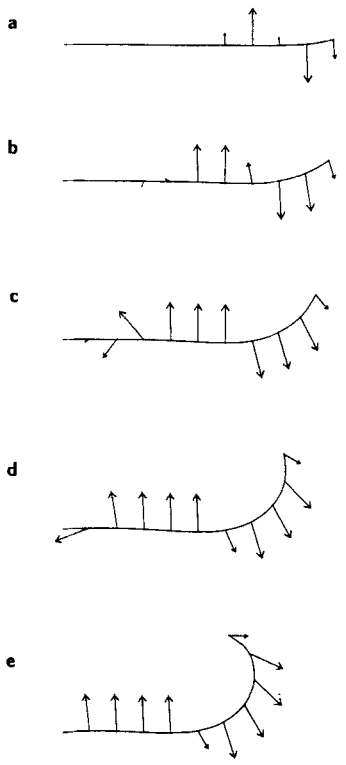

Figure 3. Lateral compression of a cantilever beam subject to end moment: Deformed configurations and friction forces at nodes for $\nu_F = 0{\cdot}05$. (a) $M/M_0 = 0{\cdot}20$; (b) $M/M_0 = 0{\cdot}40$; (c) $M/M_0 = 0{\cdot}60$; (d) $M/M_0 = 0{\cdot}80$; (e) $M/M_0 = 1{\cdot}00$

friction are depicted in Figure 2. Depending on the lateral compression and coefficient of friction, the frictional forces strongly influence the shape of the final equilibrium configurations. Figures 3 and 4 show the equilibrium configurations and frictional forces at nodes throughout the process of loading, for coefficient of friction $v_F = 0{\cdot}05$ and $v_F = 0{\cdot}02$, respectively. It is important to observe that the frictional forces are continuously changing in magnitude and direction which creates severe complexities for the numerical algorithm.

All results in this example are obtained by applying equal increments of the end moment M and automatically reducing the step if convergence is not obtained within 10 iterations. A standard check for residual norm with convergence tolerance RTOL $= 1{\cdot}0 \times 10^{-3}$ is performed. The number of load increments required to attain the final equilibrium configuration corresponding to $M/M_0 = 1{\cdot}0$, as a function of the coefficient of friction v_F, is given in Table II. It should be noted that the number of loading increments reaches highest value for the medium value of the friction coefficient $v_F = 0{\cdot}030$ which is connected with the appearance of large incremental

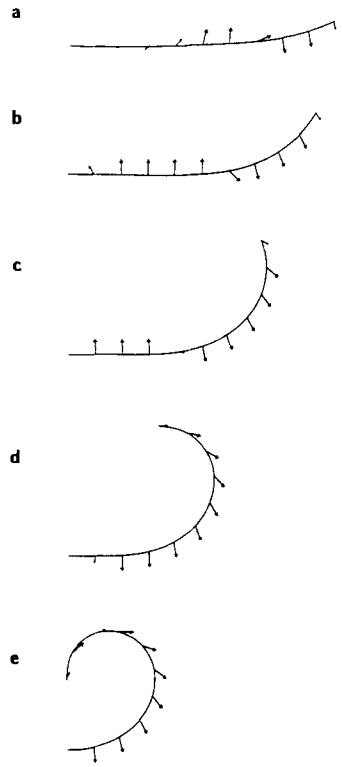

Figure 4. Lateral compression of a cantilever beam subject to end moment: Deformed configurations and friction forces at nodes for $v_F = 0{\cdot}02$. (a) $M/M_0 = 0{\cdot}20$; (b) $M/M_0 = 0{\cdot}40$; (c) $M/M_0 = 0{\cdot}60$; (d) $M/M_0 = 0{\cdot}80$; (e) $M/M_0 = 1{\cdot}00$

Table II. Number of loading increments for various v_F in Example 1

v_F	0·300	0·100	0·050	0·030	0·020	0·010	0·001
n_{inc}	20	34	29	55	36	34	21

displacements complemented with the frequent interchanges between stick and slip conditions. The speed of convergence of the Newton–Raphson method measured in residual norms is illustrated for two typical load steps in Table III. Due, probably, to the fact that within our approach (see Reference 25 for details) the rotational field for the finite element employed is not consistently linearized (as has been done in Reference 5) the apparent rate of convergence appears to be superlinear.

Example 2. Plane strain stretching of a thin sheet by a cylindrical punch

The geometry and material characterization for this example are shown in Figure 5. The analysis is performed employing a 3-D formulation, restricting the deformations to be symmetric along the line $X_1 = 0$ and imposing plane-strain boundary conditions in direction X_2. This problem, typical for thin sheet metal forming applications, is solved by discretizing the blank with 240 thin-shell finite elements and using 122 and 64 triangular flat elements to discretize the

Table III. Residual norms for two typical load steps in Example 1

n_{it}	$v_F = 0{\cdot}3$ $(M/M_0 \approx 0{\cdot}3)$	$v_F \approx 0{\cdot}05$ $(M/M_0 = 0{\cdot}3)$
1	0·124E − 01	0·622E − 02
2	0·128E − 01	0·129E − 01
3	0·171E − 03	0·239E − 03
4	0·226E − 04	0·154E − 04
5	0·804E − 06	0·617E − 06

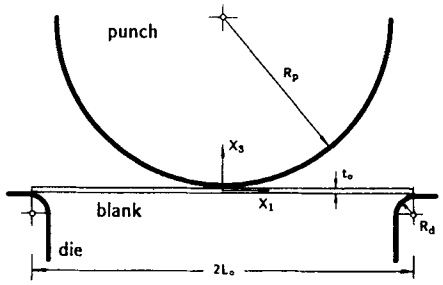

Geometry:
$L_o = 59.18$mm
$B_o = 4.0$mm
$t_o = 1.2$mm
$R_p = 50.8$mm
$R_d = 6.35$mm
Material properties:
$E = 2.1 \times 10^5$ N/mm^2
$\nu = 0.3$
$\bar{\sigma} = 520 \cdot (3.28 \cdot 10^{-4} + \bar{\varepsilon}^p)^{0.25}$N/mm^2
Boundary conditions:
Fixed displacement U_2

Figure 5. Plane strain stretching of a thin sheet by a cylindrical punch: geometry and material characteristics

surfaces of the punch and die, respectively. Spatial discretization of the problem is depicted in Figure 6. Results are obtained for the no-friction case and for a coefficient of friction $v_F = 0{\cdot}3$. Figure 7 gives deformed meshes for different values of punch displacement. Although friction does not influence the overall deformation energy visible in Figure 8 through values of the punch force, it highly influences the deformation patterns, as can be seen in Figure 9. To attain the final deformed configuration for punch displacement $D_p = 0{\cdot}5L$ with convergence tolerance

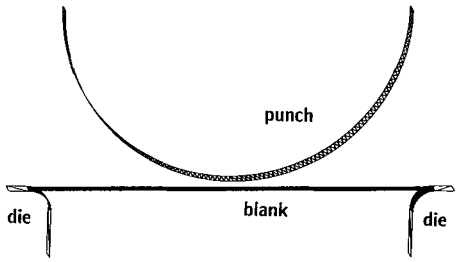

Figure 6. Plane strain stretching of a thin sheet by a cylindrical punch: Spatial finite element discretization of blank and punch and die surfaces

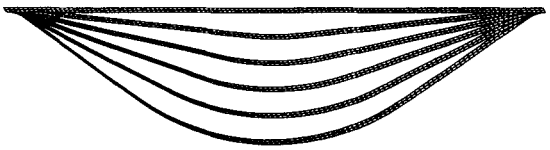

Figure 7. Plane strain stretching of a thin sheet by a cylindrical punch: Deformed finite element meshes at various stages of punch displacement. Each quadrilateral consists of two triangles

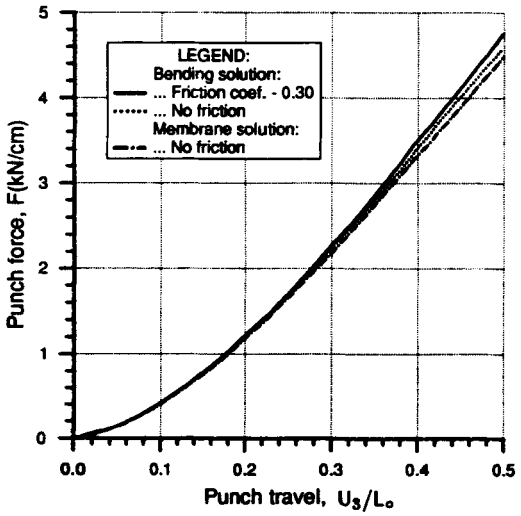

Figure 8. Plane strain stretching of a thin sheet by a cylindrical punch: Punch force versus punch displacement curves for frictionless membrane solution and for bending solution with $v_F = 0{\cdot}30$ and no friction case. Membrane solution is taken from Lee *et al.*[15]

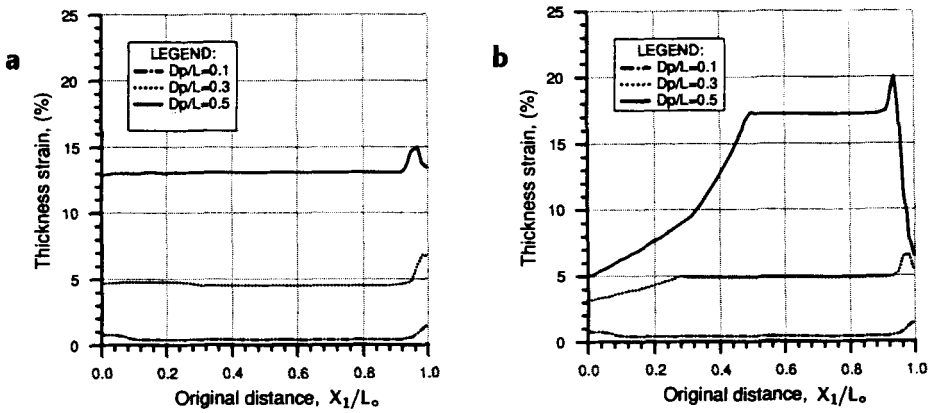

Figure 9. Plane strain stretching of a thin sheet by a cylindrical punch: Distribution of thickness true strain plotted over the initial configuration at various stages of punch displacement. (a) no friction; (b) $v_F = 0{\cdot}30$

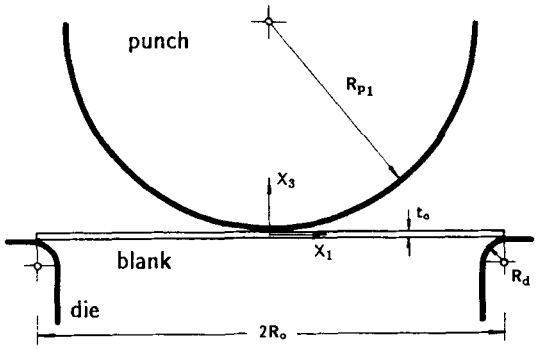

Geometry:
$R_o = 59.18\text{mm}$
$t_o = 1.0\text{mm}$
$R_{P1} = 50.80\text{mm}$
$R_{P2} = 33.90\text{mm}$
$R_d = 6.35\text{mm}$
Material properties:
$E = 69004\,\text{N/mm}^2$
$\nu = 0.3$
$\bar{\sigma} = 589 \cdot (1.0 \cdot 10^{-4} + \bar{\epsilon}^p)^{0.216}\,\text{N/mm}^2$

Figure 10. Stretching of a circular thin sheet by an elliptical punch: geometry and material characteristics

RTOL $= 1{\cdot}0 \times 10^{-3}$ for the case $v_F = 0{\cdot}3$, a total number of 68 increments of punch displacement were needed with 4–7 iterations per increment.

Example 3. Stretching of a circular thin sheet by an elliptical punch

The geometry and material characteristics for this example are shown in Figure 10. The elliptical punch surface is defined in the initial configuration by $(X_1/59{\cdot}18)^2 + (X_2/39{\cdot}45)^2$

$+ [(X_3 - 59{\cdot}18)/59{\cdot}18]^2 = 1$ with *minor axis/major axis* $= 2/3$. The analysis is performed employing a 3-D formulation, restricting the deformations to be symmetric along the lines $X_1 = 0$ and $X_2 = 0$. This problem can be considered as an intermediate stage in the forming of thin sheet metal products where the geometry of the punch initiates a behaviour which deviates from axisymmetric conditions. From a numerical point of view this necessitates full three-dimensional analysis with appropriate algorithmic treatment of the contact problem with friction. To solve this problem we discretize the blank with 736 constant-strain triangular finite elements and use 2145 and 612 triangular flat elements to discretize the surfaces of the punch and die, respectively. Spatial discretization of the problem is depicted in Figure 11. Results are obtained for coefficients

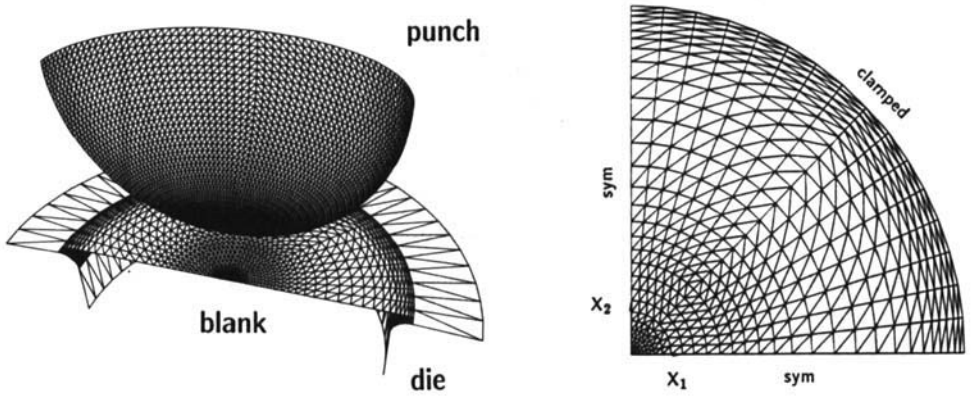

Figure 11. Stretching of a circular thin sheet by an elliptical punch: (a) Spatial finite element discretization of blank and punch and die surfaces; (b) Finite element mesh and boundary conditions for the model of the blank employed in computation

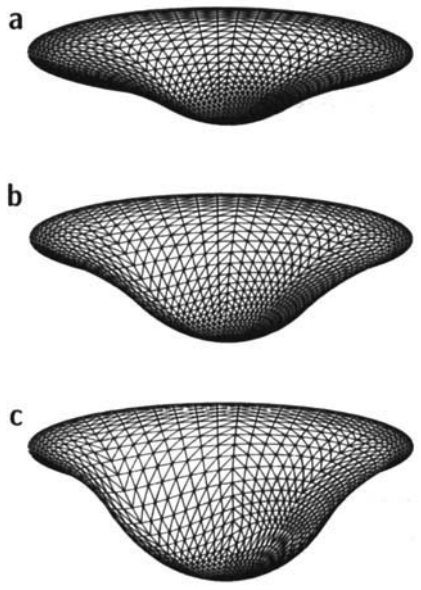

Figure 12. Stretching of a circular thin sheet by an elliptical punch: Deformed finite element meshes at various stages of punch displacement for $\nu_F = 0{\cdot}30$. (a) $D_p = 20$ mm; (b) $D_p = 30$ mm; (c) $D_p = 40$ mm

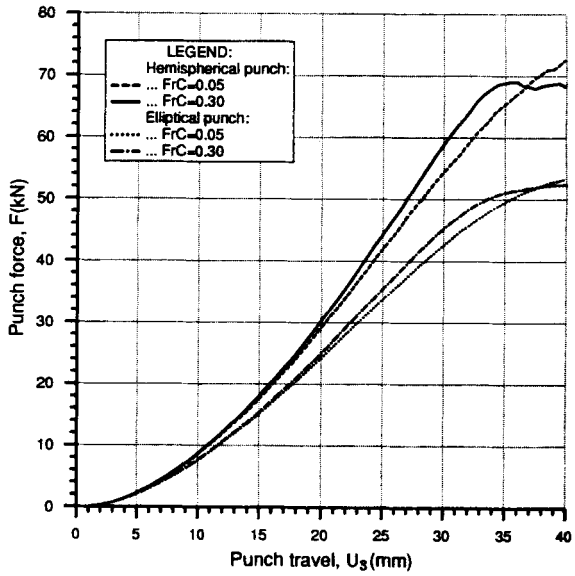

Figure 13. Stretching of a circular thin sheet by an elliptical punch: Punch force versus punch displacement curves for hemispherical and elliptical punch with $\nu_F = 0{\cdot}30$ and $0{\cdot}05$

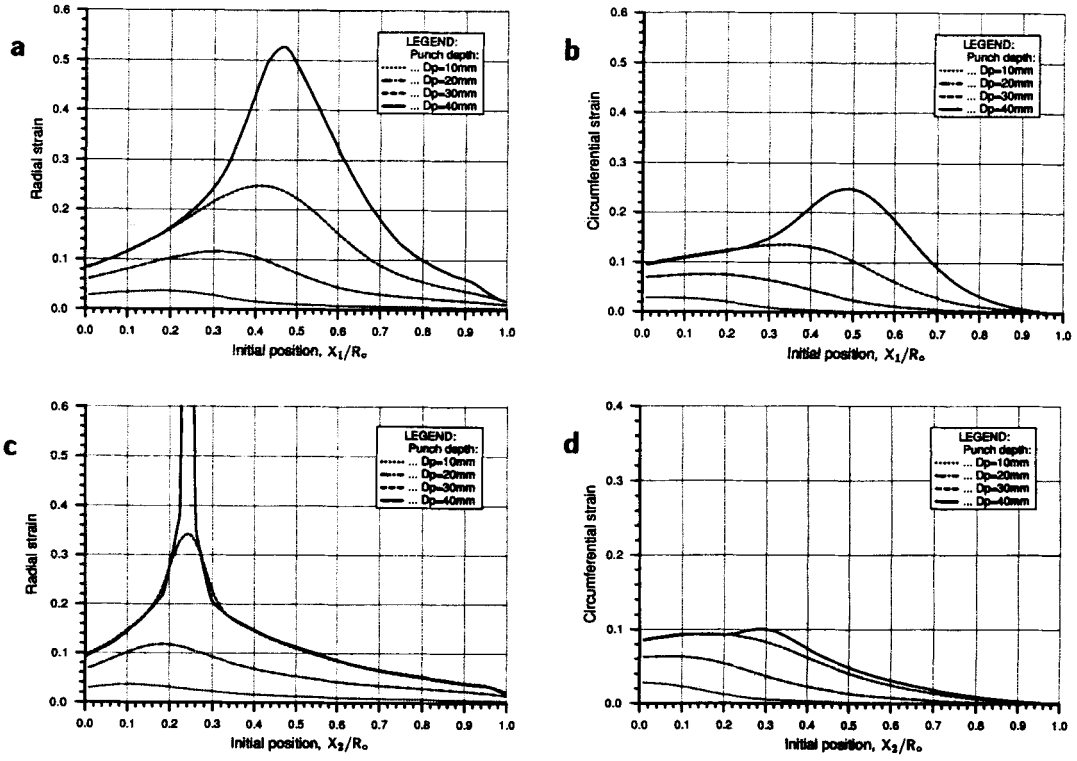

Figure 14. Stretching of a circular thin sheet by an elliptical punch: Distribution of true strain in directions X_1 and X_2 for $\nu_F = 0{\cdot}30$ plotted over the initial configuration at various stages of punch displacement. (a) X_1-radial strain, (b) X_1-circumferential strain; (c) X_2-radial strain, (d) X_2-circumferential strain

of friction $\nu_F = 0{\cdot}30$ and $0{\cdot}05$. Figure 12 gives the deformed meshes for different values of punch displacement for the $\nu_F = 0{\cdot}30$ case.

The punch force versus punch displacement diagram presented in Figure 13 gives a comparison between the results obtained by stretching a circular sheet with an elliptical punch and those obtained by hemispherical punch stretching with a spherical radius identical to the major radius of the elliptical punch. Both punch geometries were tested for $\nu_F = 0{\cdot}30$ and $0{\cdot}05$. Only a minor influence of the friction coefficient on the deformation energy can be observed with a pronounced effect on the maximum value of the punch force. Significant difference between the corresponding punch force values in hemispherical and elliptical punch stretching signals a uniform strain distribution and economical usage of material based on predominant biaxial stress states in hemispherical punch stretching.

The true strain distribution along the major and minor axes is shown in Figures 14 and 15, respectively, for various punch displacements. Overall, the strain distribution follows trends typical for an equivalent axisymmetric hemispherical punch stretching problem, with a slight increase of the strain level along the minor axis. For $\nu_F = 0{\cdot}30$ and for punch displacement $D_p > 30$ mm, we observe from Figure 14(c), a typical localization behaviour along the minor axis where strain accumulates in a narrow zone, reaching high levels and leading to failure. Spread of the localization zone is depicted in Figure 16(b), which shows the contour plots of thickness over the initial configuration. The appearance of localization and the associated failure of the circular

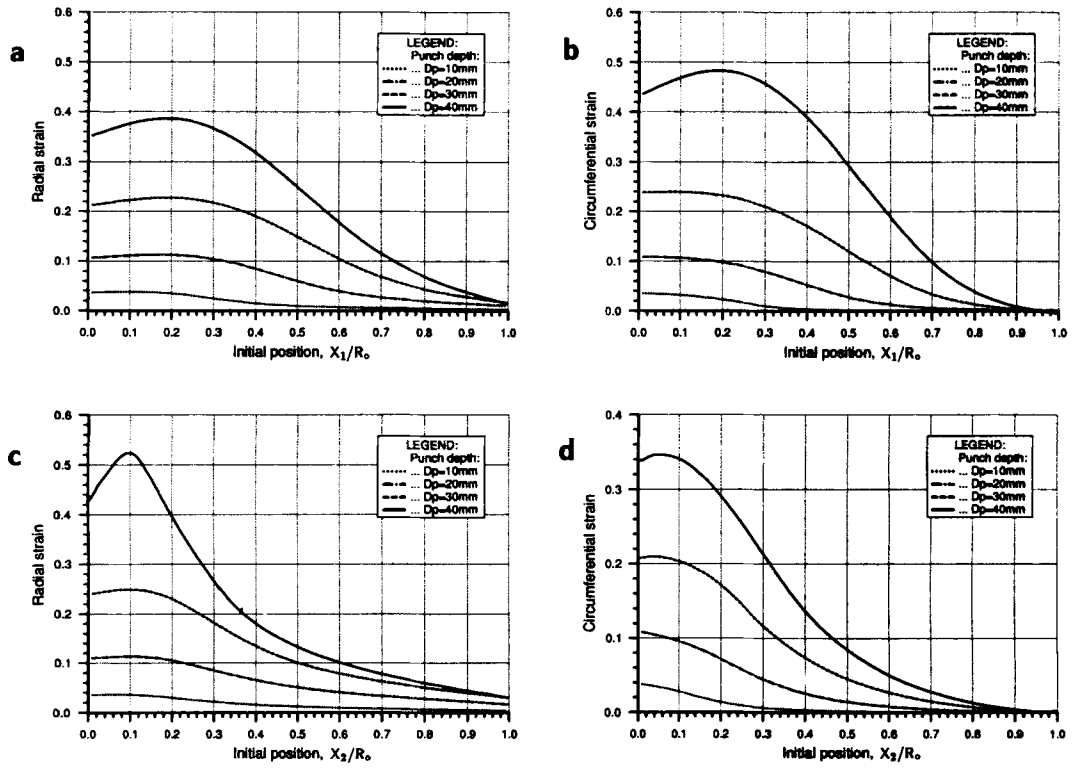

Figure 15. Stretching of a circular thin sheet by an elliptical punch: Distribution of true strain in directions X_1 and X_2 for $\nu_F = 0{\cdot}05$ plotted over the initial configuration at various stages of punch displacement. (a) X_1-radial strain, (b) X_1-circumferential strain; (c) X_2-radial strain, (d) X_2-circumferential strain

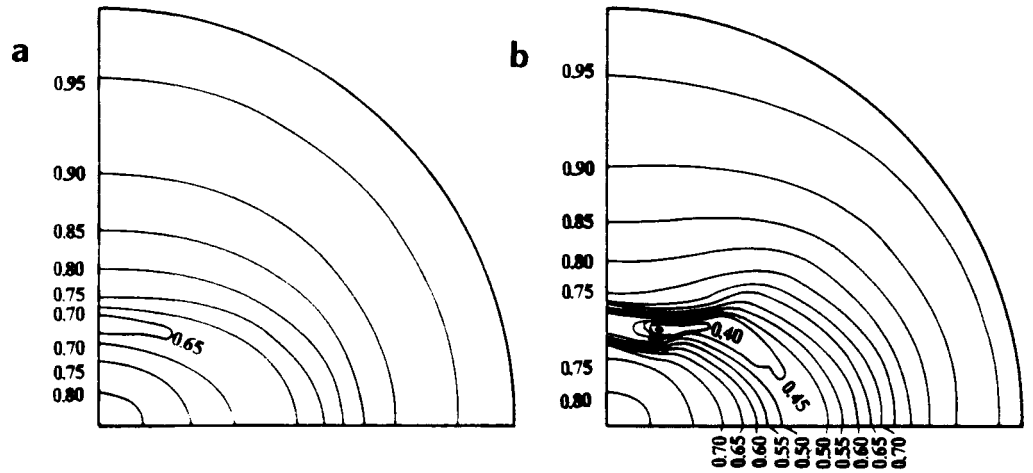

Figure 16. Stretching of a circular thin sheet by an elliptical punch: Contour plots of thickness for $v_F = 0{\cdot}30$ plotted over the initial configuration at various stages of punch displacement. (a) $D_p = 30$ mm; (b) $D_p = 40$ mm

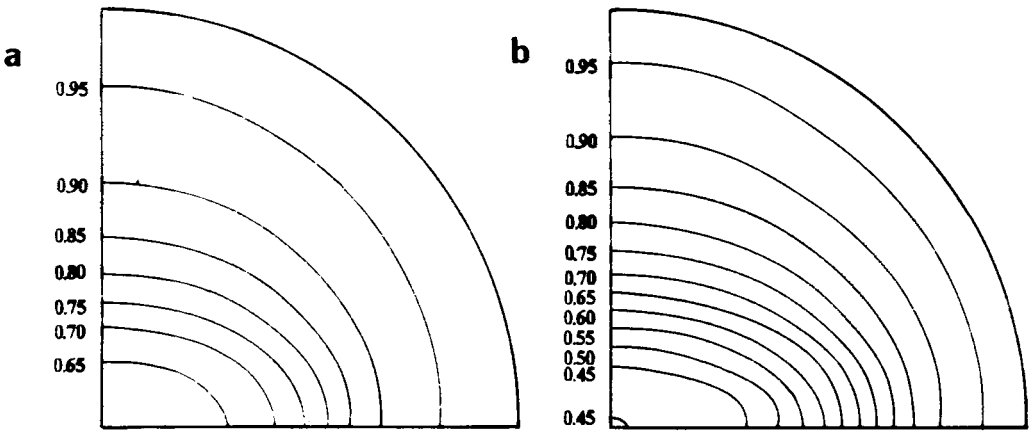

Figure 17. Stretching of a circular thin sheet by an elliptical punch: Contour plots of thickness for $v_F = 0{\cdot}05$ plotted over the initial configuration at various stages of punch displacement. (a) $D_p = 30$ mm; (b) $D_p = 40$ mm

thin sheet stretched by the elliptical punch prior to a similar failure of the thin sheet stretched by the hemispherical punch may be explained by a relaxation of conditions of axisymmetry which are known to suppress localization. We note that the early appearance of strain localization close to the minor axis of the elliptical punch gradually spreads in the circumferential direction, while in the hemispherical punch stretching strain localization appears abruptly in the whole ring of finite elements which is in an identical stress state. For $v_F = 0{\cdot}05$, although high strain levels are achieved as depicted in Figure 15, no localization is detected up to $D_p = 40{\cdot}0$ mm. This results in a uniform thickness distribution (see Figure 17) which is the objective of industrial thin sheet forming operations.

A standard check of the residual forces based on the Euclidean norm was performed in this example with convergence tolerance RTOL = $1{\cdot}0\times10^{-5}$ and $1{\cdot}0\times10^{-7}$ for the case $\nu_F = 0{\cdot}30$ and 0·05, respectively. To satisfy these convergence tolerances 4–8 iterations were typically needed. The final configuration corresponding to a punch displacement $D_p = 40{\cdot}0$ mm is attained with a total number of 159 and 112 increments for the case $\nu_F = 0{\cdot}30$ and 0·05, respectively. From Table IV, which shows the required number of loading increments corresponding to the total value of the punch displacement D_p, it can be seen that the number of increments grows as the punch displacements D_p increase beyond 30·0 mm. This is more pronounced for the $\nu_F = 0{\cdot}30$ case, which is connected with an emerging localization pattern of deformation. The rate of convergence of the Newton–Raphson method measured in residual norms is illustrated for four typical load steps in Tables V and VI. Whenever the solution is within the radius of convergence, a quadratic rate of asymptotic convergence is exhibited. We note that line searches were not performed in these examples. Finally, it should be emphasized that the present algorithm allows for new nodes entering contact at any iteration within the increment which is reflected in a sudden

Table IV. Number of loading increments for various punch displacements D_p in Example 3

D_p (mm)	5·0	10·0	15·0	20·0	25·0	30·0	35·0	40·0
n_{inc} ($\nu_F = 0{\cdot}05$)	13	23	33	43	53	63	80	112
n_{inc} ($\nu_F = 0{\cdot}30$)	14	24	36	47	57	77	119	159

Table V. Residual norms for four typical load steps for $\nu_F = 0{\cdot}30$ in Example 3

n_{it}	$D_p = 10{\cdot}0$ mm	$D_p = 20{\cdot}0$ mm	$D_p = 35{\cdot}0$ mm	$D_p = 40{\cdot}0$ mm
1	0·688E − 01	0·428E − 01	0·675E − 01	0·795E − 01
2	0·628E − 01	0·440E − 01	0·485E − 01	0·757E − 01
3	0·185E − 01	0·229E − 01	0·658E − 01	0·128E + 00
4	0·910E − 03	0·667E − 03	0·494E − 02	0·113E − 01
5	0·790E − 05	0·751E − 04	0·547E − 03	0·939E − 02
6		0·516E − 06	0·299E − 04	0·567E − 03
7			0·740E − 07	0·181E − 03
8				0·467E − 06

Table VI. Residual norms for four typical load steps for $\nu_F = 0{\cdot}05$ in Example 3

n_{it}	$D_p = 10{\cdot}0$ mm	$D_p = 20{\cdot}0$ mm	$D_p = 30{\cdot}0$ mm	$D_p = 40{\cdot}0$ mm
1	0·714E − 01	0·810E − 01	0·134E + 00	0·134E + 00
2	0·548E − 01	0·834E − 01	0·107E + 00	0·931E − 01
3	0·230E − 01	0·451E − 01	0·133E + 00	0·266E + 00
4	0·585E − 01	0·244E − 02	0·148E − 01	0·221E − 01
5	0·162E − 04	0·118E − 03	0·191E − 02	0·110E − 02
6	0·284E − 06	0·108E − 06	0·510E − 04	0·502E − 02
7	0·867E − 08	0·515E − 10	0·648E − 07	0·125E − 04
8				0·258E − 07

increase in the residual norm (as may be observed for iteration 3 of $D_p = 40{\cdot}0$ mm from Table V) and obviously destabilizes the convergence process.

7. SUMMARY AND CONCLUSIONS

A model for three-dimensional contact problems with friction based on the penalty method has been proposed and applied to the unilateral contact of flexible three-dimensional structures. Such a situation typically arises in thin sheet metal forming operations. Due to the intrinsic similarity between friction and classical elastoplasticity the constitutive model for friction can be constructed following the same formalism. This fact has been realized early and used extensively in various approaches to the solution of frictional contact problems (see e.g. References 4, 6, 8, 13, 14, 18, 27 and 33). A numerical algorithm for the plasticity theory of friction based on Wilkins'[31] radial return is described and a non-symmetric consistent tangent stiffness is derived, which has proved to be crucial for preserving the quadratic rate of convergence typical for the Newton–Raphson method.

The most important feature of the proposed algorithm is the possibility of successfully tackling the problems where sharp changes in the magnitude and direction of the frictional forces appear, as has been shown in Example 1. Although the curvature of the rigid surface is expected to influence the stability of the algorithm, in the realistic Examples 2 and 3, where frictional forces suffer continuous changes out of the tangential plane on the rigid surface, accurate and stable solutions have been achieved in a reasonable number of loading increments when the curved rigid surface has been discretized with a sufficient number of flat triangular elements.

In terms of future research we mention the possibility of including a more general constitutive model for friction and generalization to three-dimensional frictional contact problems which include non-linear contact kinematics.

ACKNOWLEDGEMENT

This work was partially funded through the BRITE initiative of the European Community (Project P-2029) and this support is gratefully acknowledged.

REFERENCES

1. D. J. Benson and J. O. Hallquist, 'A single surface contact algorithm for the post-buckling analysis of shell structures', *Comp. Methods Appl. Mech. Eng.*, **78**, 141–163 (1990).
2. G. F. Carey and J. T. Oden, *Finite Elements: A Second Course*, Prentice-Hall, Englewood Cliffs, New Jersey, 1983.
3. A. B. Chaudhary and K.-J. Bathe, 'A solution method for static and dynamic analysis of three-dimensional contact problems with friction', *Comp. Struct.*, **24**, 855–873 (1986).
4. J.-H. Cheng and N. Kikuchi, 'An incremental constitutive relation of unilateral contact friction for large deformation analysis', *J. Appl. Mech.*, **52**, 639–648 (1988).
5. M. A. Crisfield and X. Peng, 'Recent research on co-rotational beam and shell elements', in N. Bićanić *et al.* (eds.), *Nonlinear Engineering Computations*, Pineridge Press, Swansea, 1991, pp. 71–85.
6. A. Curnier, 'A theory of friction', *Int. J. Solids Struct.*, **20**, 637–647 (1984).
7. A. Curnier and P. Alart, 'A generalized Newton method for contact problems with friction', *J. Theor. Appl. Mech.*, Special issue, suppl. 1 to vol. **7**, 67–82 (1988).
8. B. Fredriksson, 'Finite element solution of surface nonlinearities in structural mechanics with special emphasis to contact and fracture mechanics problems', *Compu. Struct.*, **24**, 855–873 (1986).
9. J. O. Hallquist, G. L. Goudreau and D. J. Benson, 'Sliding interfaces with contact–impact in large-scale Lagrangian computations', *Comp. Methods Appl. Mech. Eng.*, **51**, 107–137 (1985).
10. T. J. R. Hughes, *The Finite Element Method: Linear Static and Dynamic Finite Element Analysis*, Prentice-Hall, Englewood Cliffs, New Jersey, 1987.
11. J.-W. Ju and R. L. Taylor, 'A perturbed Lagrangian formulation for the finite element solution of nonlinear frictional contact problems', *J. Theor. Appl. Mech.*, Special issue, suppl. 1 to vol. **7**, 1–14 (1988).

12. J. J. Kalker, 'Mathematical models of friction for contact problems in elasticity', *Wear*, **113**, 61–77 (1986).
13. N. Kikuchi and J. T. Oden, *Contact Problems in Elasticity: A Study of Variational Inequalities and Finite Element Methods*, SIAM, Philadelphia, 1988.
14. A. Klarbring, 'Derivation and analysis of rate boundary-value problems of frictional contact', *Eur. J. Mech., A/Solids*, **1**, 53–85 (1990).
15. J. H. Lee, S. Coudhry, J. Hambrecht and R. H. Wagoner, 'Plane strain and axisymmetric finite element investigation of sheet metal forming processes', in *Advanced Technology of Plasticity 1990*, 1389–1396, Japan Society for Technology of Plasticity, 1990.
16. J. E. Marsden and T. J. R. Hughes, *Mathematical Foundations of Elasticity*, Prentice-Hall, Englewood Cliffs, New Jersey, 1983.
17. R. M. McMeeking and J. R. Rice, 'Finite-element formulations for problems of large elastic–plastic deformation', *Int. J. Solids Struct.*, **11**, 601–616 (1975).
18. R. Michałowski and Z. Mroz, 'Associated and non-associated sliding rules in contact friction problems', *Arch. Mech.*, **30**, 259–276 (1978).
19. G. P. Mitchell and D. R. J. Owen, 'Numerical solution for elastic–plastic problems', *Eng. Comp.*, **5**, 274–284 (1988).
20. J. T. Oden and J. A. C. Martins, 'Models and computational methods for dy namic friction phenomena', *Comp. Methods Appl. Mech. Eng.*, **52**, 527–634 (1985).
21. D. R. J. Owen and E. Hinton, *Finite Elements in Plasticity*, Pineridge Press, Swansea, 1980.
22. H. Parisch, 'A consistent tangent stiffness matrix for three-dimensional non-linear contact analysis', *Int. j. numer. methods eng.*, **28**, 1803–1812 (1989).
23. D. Perić, 'On consistent stress rates in solid mechanics: computational implications', *Int. j. numer. methods eng.*, **33**, 799–817 (1992).
24. D. Perić, D. R. J. Owen and M. E. Honnor, 'A model for large strain elastoplasticity based on logarithmic strain: computational issues', *Comp. Methods Appl. Mech. Eng.*, **94**, 35–61 (1992).
25. D. Perić and D. R. J. Owen, 'The Morley shell element for large deformations problems: simplicity versus sophistication', in N. Bićanić *et al.* (eds.), *Nonlinear Engineering Computations*, Pineridge Press, Swansea, 1991, pp. 121–142.
26. N. Rebelo, J. C. Nagtegaal and H. D. Hibbitt, 'Practical aspects of modeling sheet forming processes', in E. G. Thomson *et al.* (eds.), *Numiform 89: Numerical Methods in Industrial Forming Processes*, Balkema, Rotterdam, 1989, pp. 31–43.
27. T. Rodič and D. R. J. Owen, 'A plasticity theory of friction and joint elements', in D. R. J. Owen *et al.* (eds.), *Computational Plasticity II: Models, Software and Applications*, Pineridge Press, Swansea, 1989, pp. 1043–1062.
28. J. C. Simo and R. L. Taylor, 'Consistent tangent operators for rate-independent elastoplasticity', *Comp. Methods Appl. Mech. Eng.*, **48**, 101–118 (1985).
29. J. C. Simo, P. Wriggers and R. L. Taylor, 'A perturbed Lagrangian formulation for the finite element solution of contact problems', *Comp. Methods Appl. Mech. Eng.*, **50**, 163–180 (1985).
30. J. C. Simo and T. J. R. Hughes, 'General return mapping algorithms for rate-independent plasticity', in C. S. Desai *et al.* (eds.), *Constitutive Laws for Engineering Materials: Theory and Applications*, Elsevier, New York, 1987, pp. 221–231.
31. M. L. Wilkins, 'Calculation of elastic–plastic flow', in B. Adler *et al.* (eds.), *Methods in Computational Physics*, Academic Press, New York, 1964, pp. 211–263.
32. P. Wriggers and J. C. Simo, 'A note on tangent stiffness for fully nonlinear contact problems', *Commun. appl. numer. method.*, **1**, 199–203 (1985).
33. P. Wriggers, T. Vu Van and E. Stein, 'Finite element formulation of large deformation impact-contact problems with friction', *Comp. Struct.*, **37**, 319–331 (1990).
34. Z.-Z. Zhong and J. Macherle, 'A review on static contact problems', Preprint (1990).
35. O. C. Zienkiewicz, *The Finite Element Method*, 3rd edn, McGraw-Hill, London, 1977.